IRON OXIDE NANOCLUSTERS AS *IN VITRO* BIOSENSORS OF PROTEOLYTIC ACTIVITY

By

Shann C.S. Yu

Thesis

Submitted to the Faculty of the

Graduate School of Vanderbilt University

in partial fulfillment of the requirements

for the degree of

MASTER OF SCIENCE

in

Biomedical Engineering

December, 2009

Nashville, Tennessee

Approved:

Prof. Todd. D. Giorgio

Prof. Hak-Joon Sung

BIOMEDICAL ENGINEERING

IRON OXIDE NANOCLUSTERS AS *IN VITRO* BIOSENSORS OF PROTEOLYTIC ACTIVITY

SHANN C.S. YU

Thesis under the direction of Professor Todd D. Giorgio

We demonstrate a flexible, tunable scheme for synthesizing multifunctional, ultrasmall superparamagnetic iron oxide nanoparticles (USPIOs) and its application to the area of magnetic relaxation switches. USPIO cores (10nm) were functionalized with a poly(propylene sulfide)-bl-poly(ethylene glycol) (PPS-PEG) copolymer, yielding ~40nm micelles. PPS-PEG-ssDNA conjugates and fluorophore-conjugated PPS-PEG are incorporated into the micelle synthesis process, yielding ssDNA-coated magnetofluorescent particles. To form magnetic relaxation switches, we generated USPIO populations that display complementary ssDNA sequences. Mixing of complementary USPIOs leads to clustering, resulting in a significant increase in R2 magnetic relaxation. Treatment of the DNA-crosslinked USPIO clusters with restriction enzymes specific for the crosslinking sequence results in an irreversible return of R2 relaxation to baseline levels. The constructs demonstrate their utility as nanoscale sensors of restriction enzyme activity. The presented functionalization scheme can be extended to the generation of biosensors for other sources of proteolytic activity, for diagnostics and imaging applications for cancer and atherosclerosis.

Approved: Prof. Todd D. Giorgio

DEDICATION

Throughout the whole process of conducting this work, I have been fortunate to work with some of the most amazing people. I am especially indebted to my advisor and mentor, Dr. Todd Giorgio, Chair and Professor of the Department of Biomedical Engineering, from whom there has never been anything but support of my academic and career goals, and lots of dedicated time to discuss anything from science to past experiences to life in general. Much thanks also go to Dr. Hak-Joon Sung, Assistant Professor of Biomedical Engineering, who in his one semester here, has already made an impact on my development as a researcher in this field.

One of the best things about my time here at Vanderbilt so far has been the pleasure of working with labmates who have become my brothers and sisters in our short time together so far. I would like to thank Charleson Bell, Joy Garnett, Amanda Lowery, Ryan Ortega, Josh Trantum, and Michelle Lowe for some memorable times in lab and beyond; and I am looking forward to the road ahead with these great colleagues and friends. One can never say enough about a lab that has such great chemistry together, and I think we have risen above all definitions of what workplace chemistry is about.

Of course, I am most grateful for the members of my family who have been very supportive in this process. I am thankful for the best parents in the world for their love and support despite my inability to spend as much time staying in touch with as before. I am also grateful for my brother, Shaun, whose youthful, refreshing outlook on life has been very invigorating and relaxing at the same time.

Finally, I would like to thank the many friends I have had the pleasure to meet and enjoy life with in my time here at Vanderbilt so far. Your names are too many to list here, but you know who you are.

ACKNOWLEDGMENTS

This work was supported by a grant from the Department of Defense Congressionally Directed Medical Research Programs (BC076499). Dynamic light scattering, spectrofluorimetry, spectrophotometry, and TEM were conducted through the use of the core facilities of the Vanderbilt Institute of Nanoscale Sciences and Engineering (VINSE). Mass spectrometry was conducted in the VUMC Mass Spectrometry Core, and the authors thank M. Wade Calcutt for extensive technical support and discussions. Relaxation measurements were made possible through the facilities of the Vanderbilt University Institute of Imaging Science (VUIIS).

TABLE OF CONTENTS

LIST OF TABLES

LIST OF FIGURES

LIST OF ABBREVIATIONS

AF	Alexa Fluor (Invitrogen dye)
DLS	Dynamic light scattering
DMF	Dimethylformamide
ECM	Extracellular matrix
ESI-MS	Electrospray injection mass spectrometry
FITC	Fluorescein isothiocyanate
FT-IR	Fourier-transform infrared spectroscopy
MALDI-MS	Matrix-assisted laser desorption/ionization mass spectrometry
MMP	Matrix metalloproteinase
MRI	Magnetic resonance imaging
NMR	Nuclear magnetic resonance
OA	Oleic acid
PEG	Poly(ethylene glycol)
Phth	Phthalimido group
PPS	Poly(propylene sulfide)
PPS-PEG	Poly(propylene sulfide)-poly(ethylene glycol) block copolymers
ssDNA	Single-stranded DNA
TEM	Transmission electron microscopy
THF	Tetrahydrofuran
USPIO	Ultrasmall Superparamagnetic Iron Oxides

CHAPTER I

INTRODUCTION

The development and progression of a number of diseases, most notably cancer and atherosclerosis, is marked by a significant degree of proteolytic activity. These two conditions are the leading causes of death in the United States and in many developed nations worldwide. Therefore, detection of proteolytic activity using *in vitro* blood tests, or *in vivo* through imaging can potentially revolutionize the diagnosis and treatment of atherosclerosis and cancer, enabling accurate and sensitive early detection of tumors or vulnerable atherosclerotic plaques [1-3]. Indeed, the pathologic deregulation of proteases has been popularly exploited with the goals of achieving site-specific delivery of drugs and contrast agents to diseased tissue [4].

Because of their unique properties, a wide range of nanomaterials have been extensively applied for biosensing. In particular, my work focuses on the application of ultrasmall superparamagnetic iron oxides (USPIOs) to applications involving biosensing of proteolytic activity. Individual USPIO cores exhibit diameters of smaller than 100nm, and demonstrate high R_2 magnetic relaxivity, which has led to their widespread use as negative magnetic resonance (MR) contrast agents. A number of formulations, such as Feridex, have been FDA-approved for *in vivo* imaging applications [5].

In this section, the roles of proteolysis in cancer and atherosclerosis will first be described. Next, this information will be used to illustrate the design of proteolytically-responsive biosensors, and applications of such biosensors to *in vivo* imaging. The novel "smart" contrast agents stemming from this work have the capacity to revolutionize the diagnosis and imaging of atherosclerosis and cancer.

Roles of Proteolysis in Atherosclerosis and Cancer

Proteolysis is a recurring theme in molecular biology, being important in processes ranging from the regulation of intracellular signaling pathways and the larger-scale phenomena of cell-matrix interactions. Focusing on the latter, proteolysis leads to the release of growth factors and cellular signals entrapped within the extracellular matrix (ECM). These free bioactive molecules can, in turn, cause downstream phenotypical and behavioral changes in the local cell population. The abnormal upregulation of proteolytic mediators has also been signs of pathologic states, and proteolytic activity has been linked to cancer and atherosclerosis [6, 7].

Matrix metalloproteinases (MMPs) are a class of secreted or membrane-bound proteases that, as their name implies, recognize and degrade ECM proteins. Different MMPs exhibit varying levels of substrate specificity, but are generally classified based on their primary active substrate [8, 9]. The actions of MMPs on the cellular microenvironment are associated with cell proliferation and migration, angiogenesis, and inflammatory activity. In cancer and atherosclerosis, a collection of the listed biological phenomena are confirmed to be associated with various stages of disease progression. The pathologic deregulation of the expression of certain MMPs has been correlated with abnormal manifestations of such cellular phenomena [4]. For this reason, MMPs have been intensely studied as a target for molecular imaging and drug delivery [1, 2, 10-12].

MMPs are overexpressed and actively involved in the progression of almost every human cancer, correlating with tumor invasiveness and metastasis. MMPs -2, -9, and -14 all promote tumor angiogenesis by degrading ECM components, releasing entrapped angiogenic factors (e.g. VEGF), and promoting endothelial cell invasion. The same MMPs are also active in tumor cell invasion of surrounding stromal tissue and eventual intravasation [7]. The overexpression of MMP-7 in epithelial tumor cell lines results in the shedding of cell-cell adhesion molecules (e.g. E-cadherins) and other cell surface molecules, and is associated with the progression of colonic and breast tumors [9, 13]. However, not all MMPs contribute to tumor progression and invasiveness. For example, MMP-12 expression in lung and colon cancer models has been associated with host-protective anti-angiogenic effects and increased survival [7, 13, 14]. Despite this information, MMP inhibitors received much interest and were synthesized in the pharmaceuticals industry as anticancer drug candidates. However, because of these tumor-promoting and host-protective functions of MMPs as a family, MMP inhibitors have been met with very mixed results in clinical trials [1, 7, 14].

Atherosclerosis is an inflammatory disease where the accumulation of lipids and cholesterol in arterial vessel walls leads to accumulation of inflammatory cells in the vessel media, and formation of an atherosclerotic plaque. Plaques thicken over time and disrupt perfusion of downstream capillary beds, and if they occur in coronary arteries, can lead to potentially fatal hypoxic conditions [15]. While the earliest stages of plaque formation occur in infants, pathological vascular remodeling processes destabilize the plaque microenvironment and increase the likelihood of plaque rupture. Ruptured plaques are likely to cause embolism downstream, and are associated with heart attack and stroke [16]. Because MMP-mediated ECM proteolysis is central to vascular remodeling processes, MMP activity in atherosclerotic plaques is considered to be a major cause of plaque rupture. The design of MMP-targeted therapeutics is expected to yield clinical interventions that can block the vascular remodeling that precedes plaque rupture [17]. Likewise, MMP-sensitive contrast agents have been designed in order to locate plaques that are vulnerable to rupture and identify patients that are best suited for more aggressive interventions [2, 18].

In vitro tests seeking to quantify MMP levels in serum or urine are also being developed for noninvasive diagnosis of diseased states [19-21]. A recent clinical study demonstrated that increased circulating levels of MMP-2 and MMP-9 were positively correlated with incidence of myocardial infarction in patients displaying atherosclerotic plaques [19]. Similar studies have identified MMP biomarkers for specific cancers. The invasiveness of colorectal cancers was positively correlated with circulating levels of active MMP-2 [21]. Circulating MMP-9 levels were predictive of the presence of breast tumors [20].

Therefore, MMP-responsive prodrugs, contrast agents, and biosensors have received much attention in the biomedical engineering community, and are revolutionizing modern medicine. By taking advantage of differences in MMP expression and activity in pathologic versus normal states, the design of smart theranostics (therapeutics/diagnostics) enables more accurate detection of diseases, site-specific drug delivery and activity, and less invasive clinical interventions [4].

Proteolysis as a Switch for USPIO-based Biosensors in Imaging

There are several design goals that must be met by proteolytically responsive imaging biosensors for use *in vivo*. Most importantly, materials that are used in this application must be able to specifically respond to a proteolytic environment through a measurable and clinically detectable change in material and/or physical properties. Passive and active trafficking properties to diseased areas are also very important in order to ensure proximity of contrast agents or drug delivery platforms to their intended region of activity. Finally, materials for this application (and their metabolized products) must be nontoxic and biocompatible. This section focuses on the first of these three design goals.

For imaging, ultrasmall iron oxide nanoparticles (USPIOs) have been widely investigated for applications as MRI contrast agents and for probing intermolecular interactions due to their strong T2 magnetic relaxation properties [22-25]. As contrast agents, USPIOs have unique characteristics, including high detection sensitivity, relatively low toxicity, and long circulation half-lives [26, 27]. The ability to image deep tissue with good contrast makes MRI a clinically important imaging modality, compared to intravital fluorescence. In negative contrast mode, MRI imagers capably detect changes in T2 magnetic relaxation properties within tissue volumes of interest. The trafficking of USPIOs to tissue results in a concentration-dependent, detectable decrease in local T2 relaxation [12, 28].

The aggregation state of USPIOs has also been previously shown to result in changes in material T2 relaxation properties, with clustered USPIOs exhibiting significantly smaller T2 relaxation times than dispersed USPIOs [12, 29, 30]. While the physical mechanisms behind this phenomenon remain to be explored, it is important to note that a number of physicochemical USPIO-based sensors have been constructed based on this concept. These sensors include aptamer-functionalized USPIOs for biochemical sensing, thermosensitive polymer-encapsulated USPIOs for combined imaging and drug delivery, and MMP-9-responsive sensors [12, 31, 32]. These nanoparticulate sensors respond to extrinsic stimuli by changing their aggregation state, which results in a significant change in T2 magnetic relaxation time. The resulting "magnetic relaxation switch" is a clinically applicable biosensor for physicochemical stimuli of interest.

Summary

In summary, the development of proteolytically-responsive biosensors has the potential to revolutionize the treatment, imaging, and diagnosis of cancer and atherosclerosis. The development of proteolytically-responsive nanoparticle theranostics for these diseases takes advantage of previous research demonstrating nanoparticle trafficking to disease sites and site-specific drug delivery, combining these promising results into one injectable formulation. With this area being a relatively new area, there is the increasing need for nanomaterials that are suitable for this application. Recent work by our collaborators has yielded a poly(propylene sulfide)-*bl*-poly(ethylene glycol) (PPS-PEG) block copolymer that encapsulates hydrophobic anticancer drugs and delivers the drugs to oxidative microenvironments that are characteristic of intracellular processing pathways [33, 34]. In the following chapters, we demonstrate the applicability of these polymers for encapsulating USPIOs, providing a platform onto which MRI imaging of drug delivery can be realized.

CHAPTER II

SURFACE ENGINEERING OF IRON OXIDE NANOPARTICLES FOR IMMOBILIZATION OF BIOACTIVE LIGANDS

Introduction

Biocompatible, bioactive USPIO-based contrast agents must be engineered to exhibit solubility and stability in water and, in many cases, to display ligands such as proteins, peptides, or nucleic acids. In order to achieve this goal, a modular approach for functionalizing USPIOs is generally followed. Various methods for rendering USPIOs water-soluble are well-documented, including covalent methods such as silanization or the formation of micelles with polymers or phospholipids [22, 32, 35-37]. A wide range of techniques in bioconjugate chemistry can then be used to immobilize bioactive ligands onto the USPIO surface [38].

One strategy for synthesizing water-soluble USPIOs uses the coprecipitation method to yield dextran-coated USPIOs [22, 23]. USPIOs synthesized through the thermal decomposition method demonstrate superior monodispersity and can achieve smaller particle sizes than USPIOs synthesized by coprecipitation [22, 39-41]. Further, although some studies demonstrate dextran-coated USPIOs target tumors and cardiovascular plaques *in vivo* [28, 42], recent studies reveal that surface inhomogeneities in the dextran coating can lead to adsorption of plasma proteins onto the USPIO surface and consequently, rapid clearance of the USPIOs [43]. As an alternative, grafting of poly(ethylene glycol) (PEG) continues to be a popular method of yielding “stealth” properties to nanoparticle systems because the immobilized PEG chains create a steric layer that discourages particle aggregation and undesirable particle-plasma protein interactions [44, 45]. Optimization of the pharmacokinetics and targeting efficiency of USPIOs for *in vivo* applications arguably requires the ability to exert fine control over the size range of the construct, but more importantly, the suppression of opsonization that can otherwise lead to rapid clearance of USPIOs before they have achieved their objectives.

Thermal decomposition synthesis typically yields USPIO cores coated with a layer of the hydrophobic surfactant oleic acid [46]. Covalent and noncovalent methods are available to PEGylate USPIO surfaces and render them water-soluble. In recent years, the encapsulation of USPIOs in micellar structures by self-assembly with amphiphilic PEG-containing block copolymers has received attention [32, 47, 48]. Recently, extensive studies by the Hubbell group have shown that amphiphilic block copolymers of PEG and the hydrophobic poly(propylene sulfide) (PPS) can be used to generate micellar and multilamellar structures for drug delivery applications [33, 49]. These copolymers have received interest based on their unique characteristics, including a PPS block capable of undergoing a hydrophobic-hydrophilic transition in oxidative environments, resulting in environmentally-sensitive drug release [33, 50]. Though previously uninvestigated as a USPIO coating, the PPS-PEG copolymers display material properties that can lead to the construction of novel oxidation-responsive “theranostic” (therapeutic-diagnostic) agents in the near future. To add to these properties, PPS-PEG copolymers have been successfully tagged with bioactive ligands such as peptides [51]. Here, we report the broader utility of the PPS-PEG copolymer platform through the synthesis of PPS-PEG-ssDNA constructs and fluorophore-tagged PEG-PPS constructs, and the self-assembly of these constructs upon highly monodisperse USPIO cores to generate multifunctional magnetofluorescent nanoparticles (Scheme 1).

Materials & Methods

Materials

All materials and reagents were purchased from Sigma-Aldrich (St. Louis, MO) and used as purchased unless otherwise specified. Uranyl acetate stain was purchased from Electron Microscopy Sciences (Hatfield, PA). Silanes were purchased from Gelest (Morrisville, PA). Custom ssDNA sequences were purchased from Sigma-Genosys.

Characterization of polymers by NMR and mass spectrometry

Characterization of synthesized polymers was performed using NMR, MALDI-MS, and electrospray-injection mass spectrometry (ESI-MS).

^{1}H NMR spectra were obtained at 400 MHz using a 9.4T Oxford magnet operated by a Bruker AV-400 console. The main NMR probe for the instrument is a 5mm Z-gradient broadband inverse (BBI) probe with automatic tuning and matching capability

(ATM). Lyophilized, pure samples were dissolved at 10mg/mL in $CDCl_3$, then loaded into 5mm thin-wall NMR sample tubes for measurement.

Matrix-assisted laser desorption/ionization mass spectrometry (MALDI-MS) was performed on a PerSeptive Biosystems Voyager System (Applied Biosystems, Foster City, CA). To prepare polymer samples for MALDI-MS, polymers were dissolved at a concentration of 2mg/mL in THF, and mixed 1:1 by volume with 40mg/mL of the matrix material 2-(4'-Hydroxybenzeneazo)benzoic acid (HABA). 0.5nL of the resulting polymer-matrix mixture was then pipetted onto the sample holder and allowed to air dry for at least 30 min before analysis.

SCHEME 1

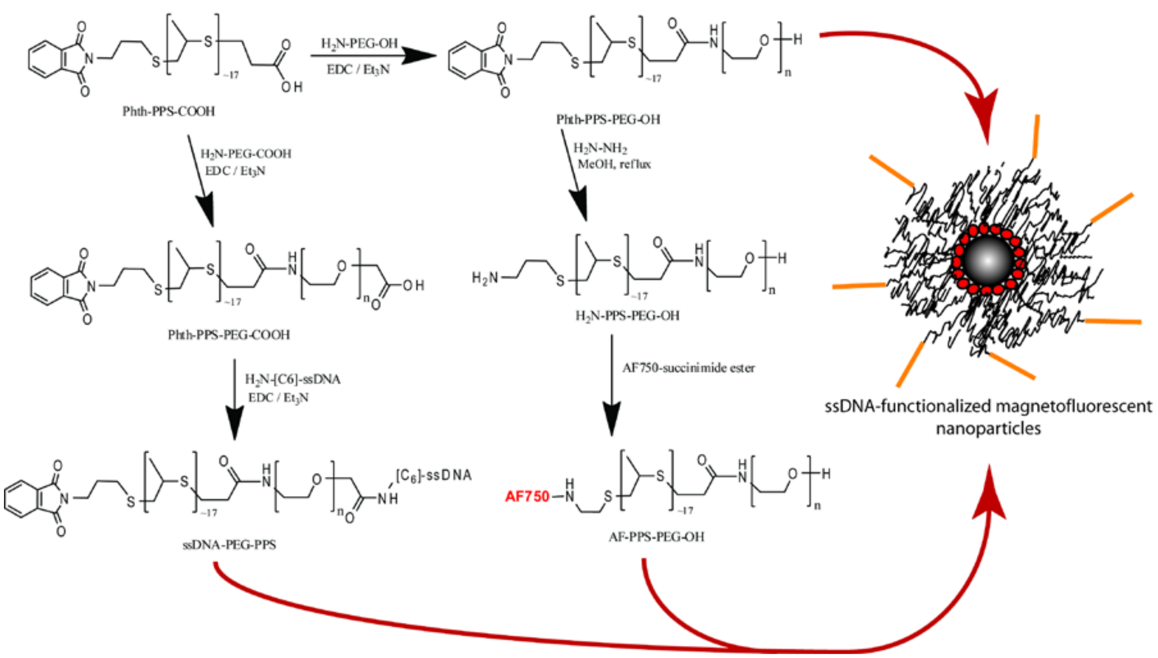

Scheme 1 – Schematic diagram of the formation of biofunctional, water-dispersible magnetofluorescent particles from amphiphilic block copolymers and hydrophobic USPIO cores. **Black fibers** = PPS-PEG copolymers, **Red** = fluorophore (AF750; AlexaFluor-750), **Yellow** = ssDNA.

Electrospray mass spectra were recorded in positive ion mode using a Synapt hybrid quadrupole/oa-TOF mass spectrometer (Waters Corp., Milford, MA) equipped with a dual chemical ionization/electrospray (ESCI) source. A post-acquisition gain correction was applied using sodium formate or sodium iodide as the lock mass. Polymer samples were reconstituted to a concentration of 1mg/mL in 1% acetic acid in THF, and then analyzed by direct injection into the mass spectrometer.

Synthesis and characterization of oleic acid-coated USPIO cores

Synthesis of 10nm diameter USPIO cores was done based on the procedures described by Woo et al. [46]. Under argon gas flow, oleic acid (3.8mL, 12 mmol) was heated to 100°C in 40mL octyl ether in a three-neck flask. $Fe(CO)_5$ (0.8mL, 6 mmol) was then injected into the system, and the mixture was then refluxed at 280°C for 4 h. Next, the mixture was cooled to 80°C and aerated overnight (>14h). The mixture was then refluxed for 2 h at 280°C and then cooled back to room temperature. USPIOs were collected following three washes in ethanol and centrifugation, and air dried overnight to form a dark brown-black powder.

Transmission electron microscopy (TEM) was conducted using a Philips CM20. Diluted USPIOs in toluene were dropped onto a carbon-coated copper grid (Electron Microscopy Sciences, Hatfield, PA) and dried naturally. This process was repeated three times. Images were collected using a CCD camera with AMT Image Capture Engine software (Advanced Microscopy Techniques, Danvers, MA), and sizing of the particles was automated using an ImageJ particle analyzer.

Synthesis of Phth-PPS-COOH

The phthalimide-protected PPS block was synthesized via anionic ring opening polymerization of propylene sulfide from a thioacetate-derivatized phthalimide initiator (Scheme 2). To form the initiator, 2.0g N-(3-acetylthiopropyl)phthalimide (7.6 mmol) was mixed in 40mL dry DMF in a Schlenk tube, and deprotected by addition of 1.05eq of 0.5M sodium methoxide in methanol (9.06mL, 7.98mmol). The tube was evacuated via a membrane pump and equilibrated with argon 5x, and then stirred at room temperature for 20 min. In this step, the color of the mixture changes from bright yellow to yellow-orange. Monomer was then added to the vessel by injection of 17eq propylene sulfide (10.18mL, 130 mmol) into the vial, and polymerization occurred for 90 min. In a separate Schlenk tube, acrylic acid (10.42mL, 152 mmol) was mixed with 13.24mL triethylamine (Et_3N; 95 mmol), resulting in the evolution of a thick white gas. This vial was evacuated via a membrane pump and equilibrated with argon gas 5x, and then the contents were transferred under vacuum into the PPS-containing vial. Upon mixing of the two liquids, a color change is observed from yellow-orange to light yellow. This

SCHEME 2

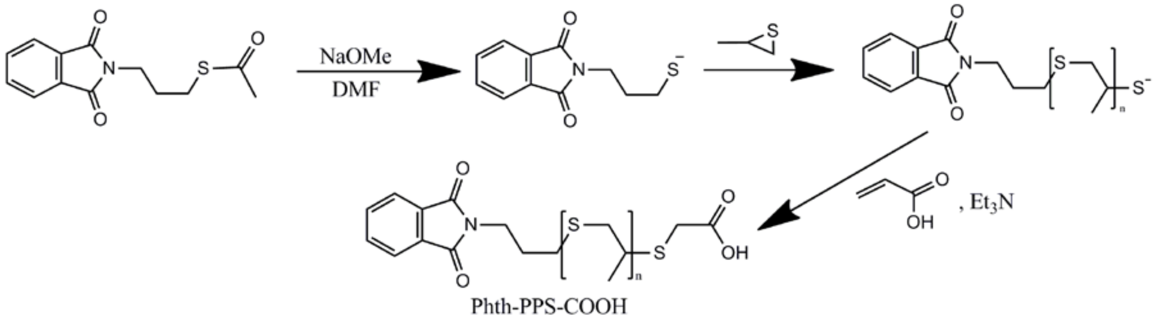

Scheme 2 – Synthesis of Phth-PPS-COOH, the hydrophobic block of the PPS-PEG amphiphilic copolymers.

mixture is then left to stir overnight at room temperature. Concentrated product is obtained by evaporation of DMF under high vacuum, and redissolved in CH_2Cl_2 (100mL). This solution was extracted 7 times in brine. The collected organic phase was then dried over 5g of sodium sulfate, and residual salts were removed by gravity filtration through a #5 Whatman filter disc. The product was concentrated by incomplete evaporation of the CH_2Cl_2 under vacuum, and then precipitated by addition to ice-cold hexanes for 30 min. Centrifugation for 5 min at 800 x g pellets the PPS block, and the hexane extraction step and centrifugation is repeated a second time to yield phthalimide-protected PPS-COOH (Phth-PPS-COOH).

^{1}H NMR (400 MHz, $CDCl_3$): δ 1.3–1.4 (d, C**H_3** in PPS block), 1.9–2.1 (q, N-CH_2-C**H_2**-CH_2-S between PPS and phthalimide), 2.2–2.4 (t, C**H_2** next to terminal carboxylic acid), 2.5–2.8 (broad s, C**H** in PPS block), 2.8–3.1 (broad s, C**H_2** in PPS block), 3.6-3.8 (t, C**H_2** adjacent to phthalimide), 7.8–8.0 (d of q, aromatic ring in phthalimide).

Synthesis of PPS-PEG block copolymers

Standard carbodiimide chemistry was used to conjugate the PPS and PEG blocks. In a round-bottom flask, 250mg of Phth-PPS_{17}-COOH (~1.5kDa), 100mg of 3kDa H_2N-PEG-OH (1.25:1 PPS:PEG), 5eq of 1-ethyl-3-(3-dimethylaminopropyl)carbodiimide (EDC; 33mg), and 5.7µL of Et_3N are mixed in 5mL dry DMF for 2 h at room temperature under argon gas. The product was concentrated by evaporation of DMF under vacuum. After redissolving in CH_2Cl_2, the product was precipitated twice in ice-cold diethyl ether

(Fisher Scientific, Pittsburgh, PA) and pelleted by centrifugation at 800 x g for 5 min. After removing the CH_2Cl_2 by vacuum evaporation, the product was resuspended in water and dialyzed overnight through 30,000 MWCO dialysis tubing (Spectrum Labs, Rancho Dominguez, CA). Excess water was removed by lyophilization overnight to yield a white powder (Phth-PPS-PEG-OH). For downstream conjugation of bioactive ligands, H_2N-PEG-COOH was used in place of the H_2N-PEG-OH described above (Scheme 1), and a fivefold molar excess of PPS was used in the reaction to discourage crosslinking of individual PEG chains, resulting in Phth-PPS-PEG-COOH. ^1H NMR (400 MHz, $CDCl_3$): δ 1.3–1.4 (d, C**H₃** in PPS block), 2.1–2.3 (s, N-CH_2-C$\mathbf{H_2}$-CH_2-S between PPS and phthalimide), 2.4–2.7 (d, C**H** in PPS block), 2.8–3.0 (d, C$\mathbf{H_2}$ in PPS block), 3.3–3.4 (s, N-C$\mathbf{H_2}$ between PPS and phthalimide), 3.4–4.0 (broad t, PEG O-C$\mathbf{H_2}$C$\mathbf{H_2}$), 6.8–6.9 (s, CON**H** bridging PPS and PEG blocks), 7.8–8.0 (t, aromatic ring in phthalimide).

Synthesis of PPS-PEG-ssDNA conjugates

For ssDNA-functionalized polymers, two sequences were purchased, all with the 5’-C6-amine modification: C1 (5’-ACG TAC GTG AT↓AT CTG CAT GCA-3’) and C2 (5’-TGC ATG CAG AT↓AT CAC GTA CGT-3’). The hybridization of these two sequences forms an EcoRV cleavage site (indicated by arrows; blunt end). These sequences (~150µg, ~20 nmol provided) were conjugated with Phth-PPS-PEG-COOH using the same procedures used for the synthesis of PPS-PEG copolymers, yielding Phth-PPS-PEG-ssDNA conjugates.

Synthesis of fluorescently-tagged PPS-PEG.

To synthesize Alexa Fluor 750-functionalized copolymers (AF-PPS-PEG), 100mg Phth-PPS-PEG-OH was first deprotected by refluxing at 120ºC for 4 h in 20mL methanol containing roughly 3-fold molar excess of hydrazine hydrate. The product mixture was then concentrated under vacuum, and redispersed in 3N KOH. The polymer was extracted 7 times in CH_2Cl_2 and precipitated in ice-cold diethyl ether, yielding H_2N-PPS-PEG-OH. Confirmation of successful deprotection was done using a ninhydrin assay. The product was then dissolved in CH_2Cl_2, then reacted with Alexa Fluor 750-succinimide ester (Invitrogen, Carlsbad, CA) according to the manufacturer's instructions, under an inert gas environment. The product was collected by ice-cold ether extraction. Free dye was removed through extensive dialysis of the concentrated product in water using 10,000 MWCO dialysis tubing. Finally, lyophilization of the retentate yielded a fine, light blue powder.

Formation and physical characterization of PEG-PPS-USPIO micelles

A co-solvent evaporation method was used to generate PEG-PPS-USPIO micelles [52]. Briefly, PPS-PEG copolymers (11mg) and 2mg of oleic acid-coated USPIO cores were dissolved in 500µL THF. This solution was sonicated briefly to break apart clumps of USPIOs. The solution was then added dropwise to 3mL of HPLC-grade water with swirling, followed by evaporation of the organic solvent in a vacuum desiccator for 2h at room temperature.

To extract unbound polymer, the micelle mixture was then washed multiple times with HPLC-grade water through a 30,000 MWCO ultrafiltration centrifugal filter (Corning, Lowell, MA), at 1000 x g, for 1 h. The pellet was then magnetically isolated and washed 3 times in HPLC-grade water. The final product was resuspended in phosphate-buffered saline for further experimentation.

To form magnetofluorescent micelles displaying ssDNA, PPS-PEG-ssDNA (1mg) and AF-PPS-PEG (<1mg) was incorporated into the initial copolymer-USPIO mixture in THF before dropwise addition to water.

Micelle sizes were characterized using TEM and dynamic light scattering (DLS). To prepare micelles for TEM, copper TEM grids were dipped into aqueous mixtures containing micelles of interest and allowed to dry in a vacuum desiccator for 2h. The grids were then stained with an aqueous 3% uranyl acetate solution for 30s and then blotted dry. Samples were dried in a vacuum desiccator for 1h before imaging on TEM as described above. The hydrodynamic diameters of PEG-PPS-USPIOs were measured in PBS using a Malvern Instruments Zetasizer Nano-ZS (Malvern Instruments, Worcestershire, UK).

Fluorescence emission spectra of magnetofluorescent USPIO micelle formulations in PBS were characterized using a Jobin Yvon/Horiba Fluorolog-3 FL3-111 spectrofluorimeter (Horiba Scientific, Edison, NJ). Because the only fluorophores used for this study were Alexa Fluor 750 dyes (Invitrogen, Carlsbad, CA), samples were excited at 750nm, and emission spectra were collected from 770-850nm.

Phenanthroline assay for iron content determination

To quantify the concentration of iron in all PEG-PPS-USPIO formulations, the 1,10-phenanthroline assay was used [53]. USPIOs in PBS (50µL) were mineralized by treatment in concentrated H_2SO_4 for 30min at room temperature, resulting in a loss of the dark brownish-black color of the solution. This was followed by treatment of the mixture with 10µL 100mg/mL hydroxylammonium chloride in water and 50µL 1mg/mL 1,10-phenanthroline in water. Development of an intense orange color, corresponding to the presence of iron, is observed upon addition of 1100µL 100mg/mL sodium acetate in water. Absorbance at 510nm was measured on a Varian Cary 5000 UV-Vis-NIR spectrophotometer (Palo Alto, CA). The concentration of free iron was calculated based on a standard curve constructed using serial dilutions of ferrous ammonium sulfate (Fisher Scientific, Pittsburgh, PA) in water. Measurements of each sample were done in triplicate.

Results

Synthesis and characterization of biofunctional PPS-PEG block amphiphilic copolymers

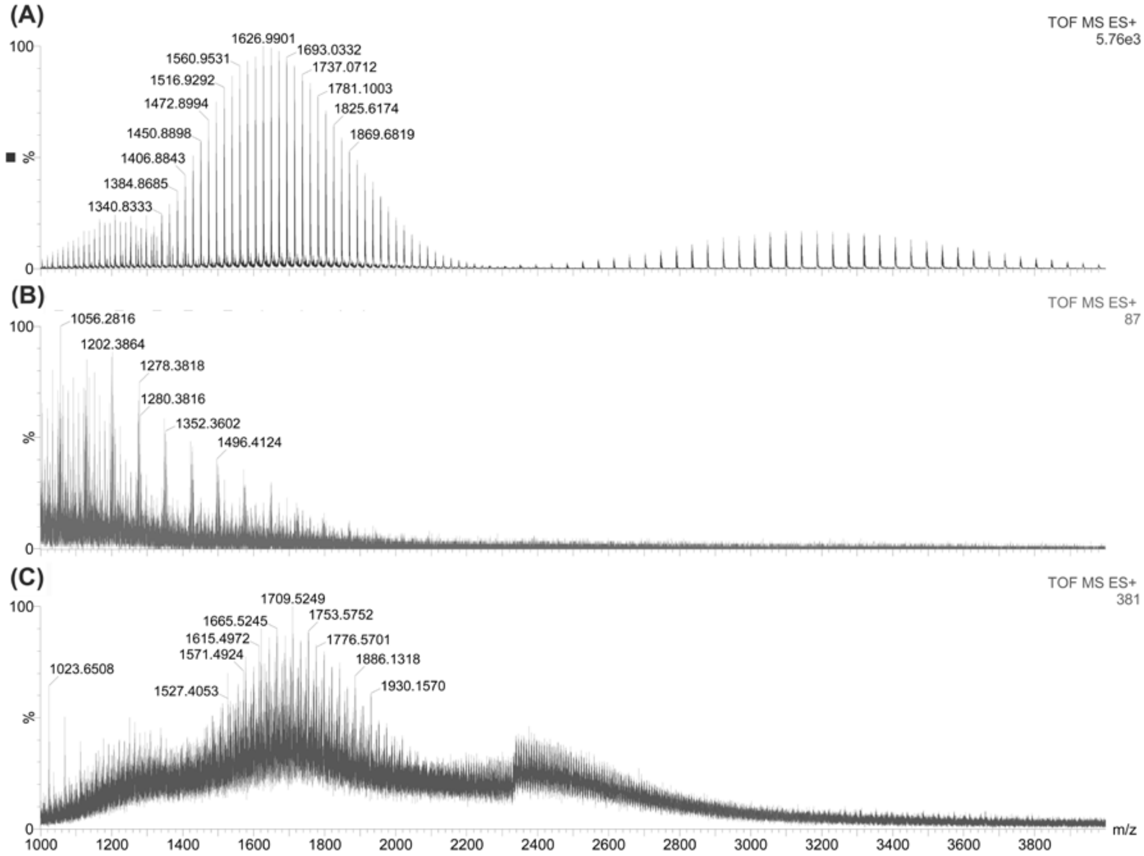

Figure 1 – ESI-MS sweeps (m/z vs. detected intensity of sample normalized as percentage of most abundantly detected substance) of PEG (A), Phth-PPS-COOH (B), and Phth-PPS-PEG-COOH (C). PEG 3000 (Sigma) spectrum is consistent with expected m/z distributions where z = +1, +2, +3. PPS spectrum is consistent with expected m/z distributions of z = +1, and peak spacing of ~74 m/z is expected of the propylene sulfide monomer. Phth-PPS-PEG-COOH spectrum is consistent with expected m/z distributions of z = +2, +3, +4. Results are consistent with successful synthesis of PPS-PEG block copolymers.

The desired PPS-PEG copolymers and derivatives, and the subsequent one-step functionalization of USPIOs, are all illustrated in Scheme 1. Conjugation of the PPS block (1.2 kDa) to the PEG block (3 kDa) was characterized by ESI-MS with 0.1% acetic acid in

THF as the mobile phase (Figure 1). Successful conjugation is noted based on the disappearance of the PEG z = +1, +2, and +3 spectra and the PPS z = +1 spectra. The peak distributions exhibited by the PPS-PEG conjugates in the m/z ranges of interest were consistent with those expected of PPS-PEG at z = +2, +3, and +4. Light scattering measurements of the polymer mixtures were performed, and the lack of any peaks suggested that the polymers did not exist in micellar form in this solvent system (data not shown).

Table 1. Physical Properties of Polymer-USPIO Micelle Formulations

Sample	**Attached DNA Sequence**[a]	**Mean Hydrodynamic Diameters ± SD (nm)**	**R_2 ± SD (mM^{-1} s^{-1})**
PEG-PPS-USPIO	-----	40 ± 5	460 ± 20
C1-USPIO	C1 (5’-ACG TAC GTG AT↓AT CTG CAT GCA-3’)	85 ± 15	460 ± 90
C2-USPIO	C2 (5’-TGC ATG CAG AT↓AT CAC GTA CGT-3’)	113 ± 23	450 ± 150
C1-USPIO + C2-USPIO	Hybridization of C1 & C2 to crosslink USPIOs	178 ± 36	690 ± 230

[a] Arrows on ssDNA sequences indicate EcoRV restriction enzyme cleavage site when sequence has hybridized with complementary ssDNA sequence.

ssDNA sequences (22 nucleotides, 6.9 kDa each) were conjugated to Phth-PPS-PEG-COOH using carbodiimide chemistry. The PPS-PEG-ssDNA conjugates were analyzed by MALDI-MS (data not shown). Successful conjugation of the sequences to the polymers was characterized by a disappearance of the 3.7 kDa band corresponding to the copolymer.

After synthesis and dialysis, AF-PPS-PEG was dissolved in water and analyzed by spectrofluorimetry. Successful synthesis of the polymer was characterized by the appearance of a fluorescence emission peak at ~810nm, with respect to the starting material (Figure 3).

PPS-PEG functionalized iron oxide-containing micelles and their physical properties

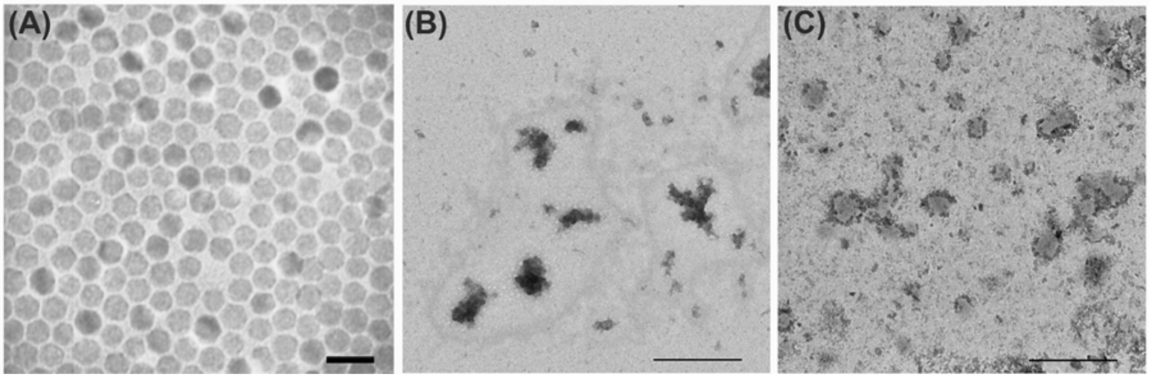

Figure 2 – High resolution TEM images of (A) 10nm USPIO cores, and the ssDNA-functionalized PPS-PEG block copolymer-encapsulated USPIO micelles designated (B) C1-USPIOs and (C) C2-USPIOs. The micelles contain aggregates of multiple USPIO cores. Scale bars = 20nm, 500nm, & 500nm, respectively.

Gram quantities of 10 ± 1nm oleic acid-coated USPIO cores were synthesized using a thermal decomposition method [46]. The cores were then deposited on a carbon grid and imaged by TEM (Figure 2a), and demonstrated regular inter-particle spacing characteristic of highly monodisperse nanoparticles. Following the functionalization with PPS-PEG copolymers, the USPIOs displayed average hydrodynamic diameters of 40 ± 5nm (Table 1). This large increase in diameter is partly due to the encapsulation of multiple USPIO cores within each micelle (Figure 2). Nevertheless, the functionalization process yields water-dispersible USPIOs that remain stable in suspension for months.

Apparently successful functionalization of OA-capped USPIOs with the block copolymer alone was extended to provide a single step synthesis of USPIOs with bioactive functionalities of interest. In this case, PPS-PEG-ssDNA constructs were incorporated into the USPIO micelles, resulting in two complementary populations of ssDNA-USPIOs referred to as C1-USPIO and C2-USPIO. The incorporation of PPS-PEG-ssDNA conjugates into micelle formation generally led to larger hydrodynamic diameters as determined by light scattering measurements (Table 1). This is evidenced by the increased average hydrodynamic diameter to approximately 100nm across all ssDNA-functionalized USPIO samples. This large increase in hydrodynamic diameter may suggest some extent of particle aggregation *in situ*, and this is confirmed by TEM images of the USPIO-containing micellar structures (Figure 2b-2c).

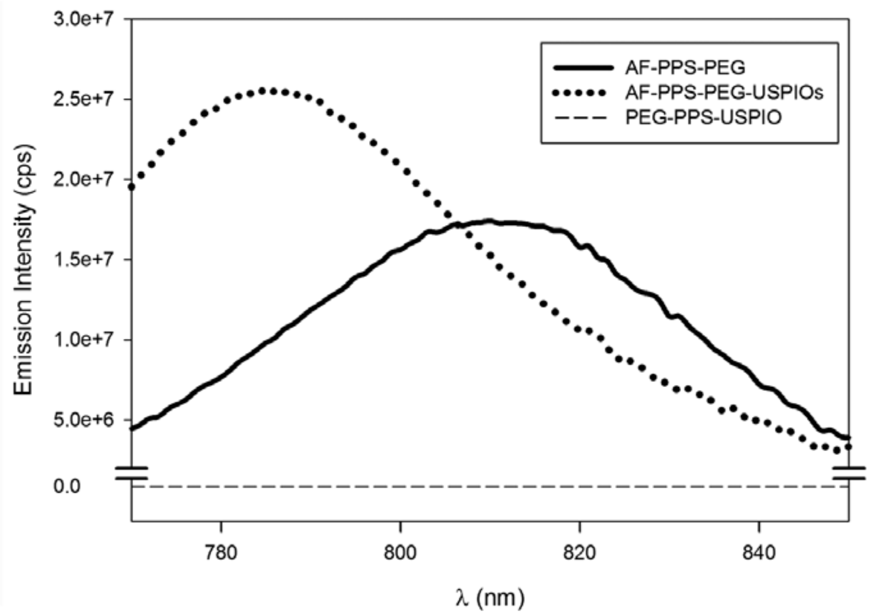

Figure 3 – Emission spectra of free AlexaFluor-tagged PPS-PEG copolymer (AF-PPS-PEG; solid) and AF-PPS-PEG incorporated into USPIO micelles (AF-PPS-PEG-USPIOs; dotted) obtained by excitation of samples at 750nm. Emission intensity is reported in arbitrary units (cps; counts per second). Spectral differences stem from the microenvironment where the AF dye is located. As a negative control, the emission spectrum of PEG-PPS-USPIO without the fluorescent tag (PEG-PPS-USPIO; dashed) is shown.

Finally, fluorescently tagged copolymer was also incorporated into the micelle formation process, resulting in magnetofluorescent USPIO micelles (Figure 3). Compared to free AF-PPS-PEG, the complexed AF-PPS-PEG exhibited a blue shift in the fluorescence emission peak from ~810nm to ~785nm.

Discussion

In this section, the flexible one-step functionalization of USPIOs with bioactive ligands and PEG was demonstrated. Highly monodisperse 10nm USPIO cores were encapsulated into >40nm micelles containing multiple cores each (Figure 2). While the micelles are less monodisperse than the original cores, this result appears to be a product of the micelle formation process. Other groups have used alternative amphiphilic block copolymers to encapsulate USPIOs and experienced similar results [32, 48]. In the cited work, the amphiphlic copolymers exhibited molecular weights above 5kDa, compared to the 1.5kDa used in the studies here. While the polymers are very different, it may be possible to exert control over micelle size and the number of USPIO cores per micelle by varying the length and molecular weight of the hydrophobic block in the amphiphilic copolymers. By significantly decreasing the length of the hydrophobic block, it may be possible to produce micelles containing single USPIO cores each, for similar reasons as self-assembled monolayer formation on gold surfaces. In this way, product micelle monodispersity is dictated solely by the monodispersity of the USPIO cores and the polydispersity index of the amphiphilic copolymers used.

Upon incorporation of AF-PPS-PEG to the USPIO micelles, a blue shift in the fluorescence emission peak was observed. This blue shift phenomenon has been previously reported for magnetofluorescent nanobeads using USPIO-quantum dot core-shell structures [54-56]. Known as the dynamic Stokes shift in solution, the phenomenon is observed when changing the microenvironment wherein fluorophores are adsorbed or dissolved [57]. Because the AF dye used in our studies was coupled to the hydrophobic block of the polymers, its physical position in the micelle is expected to be within the hydrophobic layer between the USPIO surface and the PEG corona. This microenvironment is very different from the aqueous medium used to analyze the polymers without the USPIOs present.

Given the extensive use of carbodiimide chemistry to couple bioactive ligands through a relatively stable amide linkage to the polymer backbone, the presented reaction schemes are expected to be very applicable for coupling peptides, proteins and other moieties to the polymer. From there, the micelle formation process enables the stable display of such moieties on the USPIO surface.

CHAPTER III

THE MAGNETIC RESONANCE SWITCH: ENZYMATICALLY-CLEAVABLE IRON OXIDE NANOPARTICLE CLUSTERS AS BIOSENSORS OF PROTEOLYTIC ACTIVITY

Introduction

To demonstrate the applicability of the USPIO functionalization approach described in the previous section, ssDNA-tagged USPIOs will be used as magnetic relaxation switches (MRS) [29, 30, 58]. The MRS concept indicates that clustering of USPIOs leads to a significant increase in R2 relaxivity of the USPIOs, while declustering returns relaxivity to baseline levels. The MRS label originated from the behavior of the system as a nanosensor capable of being turned on or off in the presence of a specific environmental stimulus, which, for our demonstration purposes, is restriction enzyme activity. Though the ultimate goal is to produce MMP-responsive biosensors, the USPIO functionalization scheme is flexible enough to accommodate alternative biomolecules other than ssDNA, and the presented work provides a proof of concept of the utility of our fabrication scheme for future work.

Complementary populations of ssDNA-USPIOs were mixed to form clusters. These clusters were subjected to restriction enzyme treatment or thermocycling to decluster the USPIO cores irreversibly or reversibly. Light scattering and relaxation measurements were carried out on clustered and declustered MRS in aqueous solution. Altogether, the work presented here offers a flexible platform for generating highly monodisperse, multifunctional magnetofluorescent nanoparticles that are dispersible in water and enable biosensing by modulation of image contrast.

Materials & Methods

R2 relaxation measurements

A 0.5T Maran tabletop NMR scanner with DRX-II console (Oxford Instruments, Oxfordshire, UK) was used for transverse (T_2) relaxation time measurements. 200µL of PEG-PPS-USPIOs in PBS were loaded into 5-mm thin-walled NMR tubes and introduced into the scanner. Measurements were made using a Carr-Purcell-Meiboom-Gill (CPMG) sequence at room temperature, 32 echoes with 12ms time between echoes, and an average of 9 acquisitions. R_2 relaxation coefficients were calculated based on the following formula [59], where [Fe] is the iron content of the sample as determined through the phenanthroline assay (described earlier):

$$R_2 = \frac{1}{T_2 \times [Fe]} \tag{1}$$

For clustering/declustering experiments, 100µL of complementary ssDNA-USPIO populations were mixed in the NMR tubes and allowed 10min to cluster before T_2 was remeasured as described above. To study the effects of restriction enzyme treatment, 500U of EcoRI or EcoRV were added to the tubes according to the manufacturer's instructions and the system was incubated at 37°C for 4 h before relaxation time was remeasured. To study the effects of thermocycling, samples in NMR tubes were heated to 85°C in a water bath for 15 min, then measured in the relaxometer. The temperatures in heated ssDNA-USPIO samples did not drop below 70°C during the measurement process. Unless otherwise noted, all presented data is the average of three independent experiments.

Results

Clustering of complementary USPIOs leads to increase in R_2 relaxivity coefficients

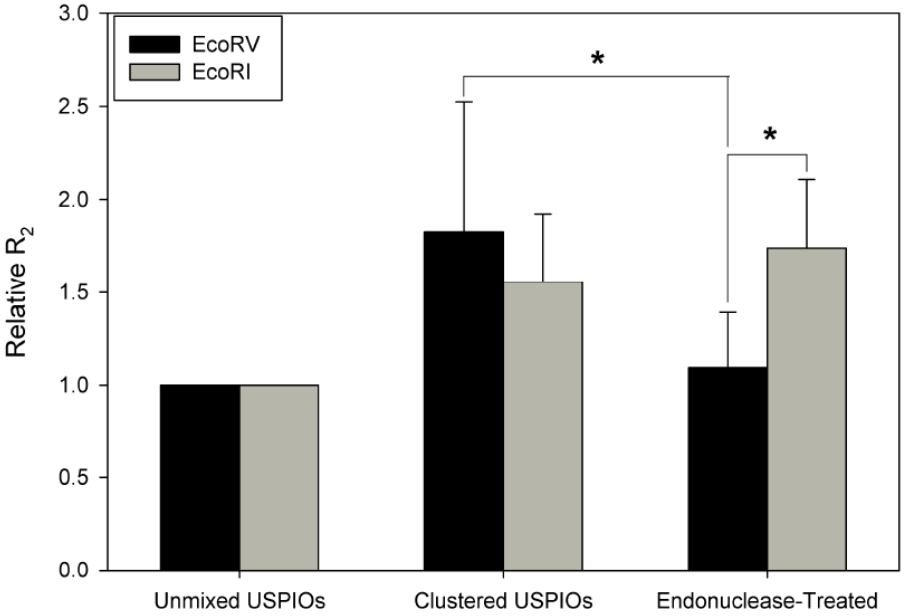

Figure 4 - Self-assembly of EcoRV-sensitive ssDNA-USPIO clusters, and subsequent enzymatic treatment results in measurable changes in R_2 relaxation coefficient normalized to initial values. Following EcoRV treatment, R_2 values return to baseline, a phenomenon that is in significant contrast to the effects of EcoRI treatment of the same clusters (n = 6). * $p < 0.05$

R_2 coefficients were calculated based on measurements of USPIO iron content through the phenanthroline assay [53] and relaxation time measurements. For all polymer-USPIO micelle samples, R_2 values ranged between 400-500 $mM^{-1} s^{-1}$ (Table 1).

When C1-USPIOs and C2-USPIOs were mixed, the hybridization of the surface-immobilized ssDNA sequences results in crosslinking of the USPIOs into larger clusters. This response is observed via an increase in hydrodynamic diameters to 178 ± 36nm, and an increase in R_2 coefficient to 690 ± 230 $mM^{-1} s^{-1}$ (Table 1).

Enzymatic treatment and thermocycling of USPIO clusters and effects on R_2

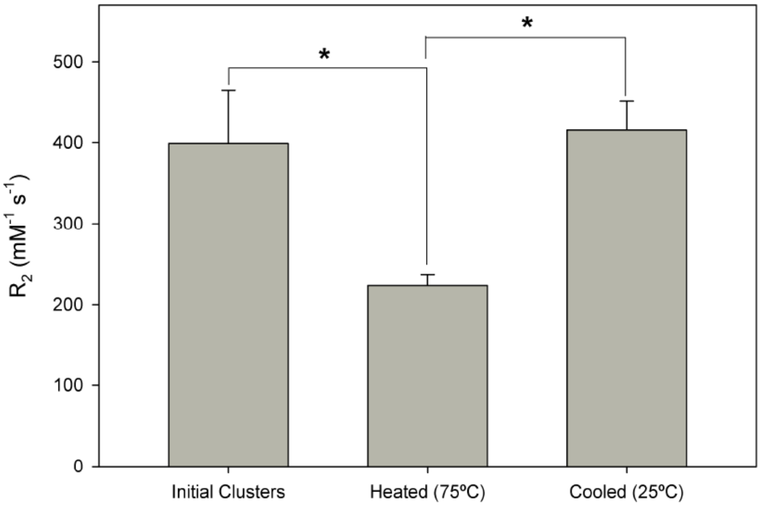

Figure 5 – Thermocycling of DNA-crosslinked USPIO clusters results in measurable changes in R_2 relaxation coefficient. Heating of the clusters melts the DNA and results in declustering of the particles, corresponding to an approximately 50% decrease in R_2 coefficient. After allowing the system to cool, the R_2 coefficient increases to original levels, suggesting the reclustering of the ssDNA-USPIOs (n = 3).

Since clustering of the complementary C1-USPIOs and C2-USPIOs resulted in expected changes in R_2, the next goal was to determine whether reversal of the clustering process would likewise correspondingly reverse the observed increase in R_2. Irreversible and reversible 'declustering' of the USPIO complexes was achieved through enzymatic treatment and through thermocycling experiments, respectively.

By design, the hybridization of USPIO-immobilized C1- and C2- sequences reveals an EcoRV blunt end cleavage site. Treatment of the clusters with EcoRV is thus expected to redisperse the individual micelles, resulting in irreversible return of the R_2 values to the baseline levels prior to the formation of the clusters. This expectation is confirmed by relaxometry data (Figure 4), where a significant difference in R_2 ($p < 0.05$) is measured following treatment with EcoRV. In contrast, clusters were alternatively treated with EcoRI as a negative control, and the lack of a declustering response is reflected in an insignificant change in the R_2 coefficient of the system.

Next, reversible declustering of the USPIOs was achieved through thermocycling, where R_2 measurements were made while the USPIO clusters were being subjected to heating and cooling. In this process, heating and cooling of the clusters melts and reanneals the crosslinking DNA sequences, respectively. The resulting changes in the clustering of USPIOs leads to expected fluctuations in R_2 (Figure 5). The heated clusters are expected to decluster, resulting in the return of R_2 values to baseline levels prior to mixing C1-USPIOs and C2-USPIOs. Allowing the system to cool is expected to reanneal the DNA sequences and reform clusters, returning R_2 levels to the ranges expected for clusters. Heating of the clusters resulted in approximately 50% decrease in R_2, while return of the system to room temperature resulted in recovery of the original R_2.

Discussion

The magnetic relaxivities of the ssDNA-functionalized particles were investigated and compared to other polymer-encapsulated USPIO formulations. The measured R2 values were well within expected ranges, and are similar in order of magnitude to those recently measured by LaConte et al and Lee et al [59, 60]. Differences in the absolute R_2 values reported are easily accounted for, since LaConte et al used USPIO cores of smaller diameters (~6nm), while Lee et al used USPIO cores that had been doped with other metals such as manganese. Upon clustering complementary ssDNA-USPIOs, a significant increase in R_2 was observed (Table 1). This phenomenon is consistent with previously published results [48][29, 48, 58, 61]. The mechanisms behind this “MRS” effect remains largely unstudied and is the subject of an ongoing study in our group.

The goal of treating USPIO clusters with restriction enzymes is to induce irreversible redispersion of the USPIO clusters. EcoRV treatment resulted in redispersed USPIOs that did not reform the original DNA-crosslinked clusters, while EcoRI treatment did not result in any significant changes in the R_2 values of the samples. In the thermocycling experiments, the data suggests that the USPIO clusters are indeed crosslinked by DNA, as the PCR-inspired thermal fluctuations subjected the clusters to reversible declustering. Our data matched the expected behavior of such a system under the subjected conditions, and the trends are within agreement with previously published results by Weissleder’s group using USPIOs functionalized through an alternative route [29, 58].

CHAPTER IV

CONCLUSIONS

Novel PPS-PEG based polymers were synthesized and characterized, then applied as a USPIO coating in a one-step co-solvent evaporation method to yield USPIO micelles. The synthesis of fluorescently tagged polymers and ssDNA-tagged polymers and the incorporation of these species into the micelle formation process leads to the relatively simple formation of multifunctional USPIO micelles. The generation of complementary populations of ssDNA-USPIOs results in a system that is capable of detecting proteolytic events through significant changes in R_2 relaxation coefficient of the system. Therefore, the presented USPIO functionalization scheme results in bioactive nanoparticulate agents that can be extended to *in vitro* and *in vivo* biosensing applications in the future.

CHAPTER V

ONGOING AND FUTURE WORK

The presented work serves as preliminary data to my ongoing work where the USPIO crosslinkers (DNA in this work) are now MMP-degradable peptides. When complete, the peptide-crosslinked USPIO micelle clusters will serve as a candidate for *in vivo* molecular imaging of MMP activity. Ongoing experiments examine the behavior of the USPIO nanoclusters *in vitro* in cultures of immune cells such as macrophages, which are among the important MMP-releasing cell types in vulnerable atherosclerotic plaques. *In vivo* experiments in murine models of atherosclerosis have been proposed for this project. These smart contrast agents will hone in on cancer tumors and atherosclerotic plaque sites, only becoming activated in the presence of proteolytic microenvironments that signify specific stages of disease. This technology will enable better diagnosis of a patient's condition and more accurate assignment of treatment options.

Further, the materials used in this study have been previously used for intracellular drug delivery, enabling the realization of a "theranostic" platform for imaging drug localization and delivery to sites of interest in the body.

BIBLIOGRAPHY

1. Scherer, R.L., J.O. McIntyre, and L.M. Matrisian, *Imaging matrix metalloproteinases in cancer.* Cancer Metastasis Rev, 2008. **27**(4): p. 679-90.

2. Fujimoto, S., et al., *Molecular imaging of matrix metalloproteinase in atherosclerotic lesions: resolution with dietary modification and statin therapy.* J Am Coll Cardiol, 2008. **52**(23): p. 1847-57.

3. Hartung, D., et al., *Targeting of matrix metalloproteinase activation for noninvasive detection of vulnerable atherosclerotic lesions.* Eur J Nucl Med Mol Imaging, 2007. **34 Suppl 1**: p. S1-8.

4. Law, B. and C.H. Tung, *Proteolysis: a biological process adapted in drug delivery, therapy, and imaging.* Bioconjug Chem, 2009. **20**(9): p. 1683-95.

5. Briley-Saebo, K.C., et al., *Fractionated Feridex and positive contrast: in vivo MR imaging of atherosclerosis.* Magn Reson Med, 2008. **59**(4): p. 721-30.

6. Galis, Z.S., et al., *Increased expression of matrix metalloproteinases and matrix degrading activity in vulnerable regions of human atherosclerotic plaques.* J Clin Invest, 1994. **94**(6): p. 2493-503.

7. Egeblad, M. and Z. Werb, *New functions for the matrix metalloproteinases in cancer progression.* Nat Rev Cancer, 2002. **2**(3): p. 161-74.

8. Parks, W.C. and R.P. Mecham, *Matrix metalloproteinases*. Biology of extracellular matrix series. 1998, San Diego: Academic Press. xii, 362 p.

9. Murphy, G. and H. Nagase, *Progress in matrix metalloproteinase research.* Mol Aspects Med, 2008. **29**(5): p. 290-308.

10. Deguchi, J.O., et al., *Inflammation in atherosclerosis: visualizing matrix metalloproteinase action in macrophages in vivo.* Circulation, 2006. **114**(1): p. 55-62.

11. Lancelot, E., et al., *Evaluation of matrix metalloproteinases in atherosclerosis using a novel noninvasive imaging approach.* Arteriosclerosis Thrombosis and Vascular Biology, 2008. **28**(3): p. 425-432.

12. Schellenberger, E., et al., *Protease-specific nanosensors for magnetic resonance imaging.* Bioconjug Chem, 2008. **19**(12): p. 2440-5.

13. McIntyre, J.O., et al., *Development of a novel fluorogenic proteolytic beacon for in vivo detection and imaging of tumour-associated matrix metalloproteinase-7 activity.* Biochem J, 2004. **377**(Pt 3): p. 617-28.

14. Martin, M.D. and L.M. Matrisian, *The other side of MMPs: protective roles in tumor progression.* Cancer Metastasis Rev, 2007. **26**(3-4): p. 717-24.

15. Sanz, J. and Z.A. Fayad, *Imaging of atherosclerotic cardiovascular disease.* Nature, 2008. **451**(7181): p. 953-7.

16. Saam, T., et al., *The vulnerable, or high-risk, atherosclerotic plaque: noninvasive MR imaging for characterization and assessment.* Radiology, 2007. **244**(1): p. 64-77.

17. Galis, Z.S. and J.J. Khatri, *Matrix metalloproteinases in vascular remodeling and atherogenesis: the good, the bad, and the ugly.* Circ Res, 2002. **90**(3): p. 251-62.

18. Trivedi, R.A., et al., *In vivo detection of macrophages in human carotid atheroma: temporal dependence of ultrasmall superparamagnetic particles of iron oxide-enhanced MRI.* Stroke, 2004. **35**(7): p. 1631-5.

19. Hlatky, M.A., et al., *Matrix metalloproteinase circulating levels, genetic polymorphisms, and susceptibility to acute myocardial infarction among patients with coronary artery disease.* Am Heart J, 2007. **154**(6): p. 1043-51.

20. Jesneck, J.L., et al., *Do serum biomarkers really measure breast cancer?* BMC Cancer, 2009. **9**: p. 164.

21. Waas, E.T., et al., *Plasma levels of matrix metalloproteinase-2 and tissue inhibitor of metalloproteinase-1 correlate with disease stage and survival in colorectal cancer patients.* Dis Colon Rectum, 2005. **48**(4): p. 700-10.

22. Jeong, U., et al., *Superparamagnetic colloids: Controlled synthesis and niche applications.* Advanced Materials, 2007. **19**(1): p. 33-60.

23. Josephson, L., et al., *High-efficiency intracellular magnetic labeling with novel superparamagnetic-Tat peptide conjugates.* Bioconjug Chem, 1999. **10**(2): p. 186-91.

24. Park, J.H., et al., *Micellar hybrid nanoparticles for simultaneous magnetofluorescent imaging and drug delivery.* Angew Chem Int Ed Engl, 2008. **47**(38): p. 7284-8.

25. Perez, J.M., L. Josephson, and R. Weissleder, *Use of magnetic nanoparticles as nanosensors to probe for molecular interactions.* Chembiochem, 2004. **5**(3): p. 261-4.

26. Cormode, D.P., et al., *Nanotechnology in Medical Imaging. Probe Design and Applications.* Arterioscler Thromb Vasc Biol, 2009.

27. Briley-Saebo, K.C., et al., *Magnetic resonance imaging of vulnerable atherosclerotic plaques: current imaging strategies and molecular imaging probes.* J Magn Reson Imaging, 2007. **26**(3): p. 460-79.

28. Nahrendorf, M., et al., *Noninvasive vascular cell adhesion molecule-1 imaging identifies inflammatory activation of cells in atherosclerosis.* Circulation, 2006. **114**(14): p. 1504-11.

29. Josephson, L., J.M. Perez, and R. Weissleder, *Magnetic nanosensors for the detection of oligonucleotide sequences.* Angewandte Chemie-International Edition, 2001. **40**(17): p. 3204-+.

30. Perez, J.M., et al., *Magnetic relaxation switches capable of sensing molecular interactions.* Nat Biotechnol, 2002. **20**(8): p. 816-20.

31. Yigit, M.V., et al., *Smart "Turn-on" magnetic resonance contrast agents based on aptamer-functionalized superparamagnetic iron oxide nanoparticles.* Chembiochem, 2007. **8**(14): p. 1675-1678.

32. Talelli, M., et al., *Superparamagnetic iron oxide nanoparticles encapsulated in biodegradable thermosensitive polymeric micelles: toward a targeted nanomedicine suitable for image-guided drug delivery.* Langmuir, 2009. **25**(4): p. 2060-7.

33. Napoli, A., et al., *Oxidation-responsive polymeric vesicles.* Nat Mater, 2004. **3**(3): p. 183-9.

34. Velluto, D., D. Demurtas, and J.A. Hubbell, *PEG-b-PPS diblock copolymer aggregates for hydrophobic drug solubilization and release: cyclosporin A as an example.* Mol Pharm, 2008. **5**(4): p. 632-42.

35. Xie, J., et al., *One-pot synthesis of monodisperse iron oxide nanoparticles for potential biomedical applications.* Pure and Applied Chemistry, 2006. **78**(5): p. 1003-1014.

36. Kohler, N., G.E. Fryxell, and M. Zhang, *A bifunctional poly(ethylene glycol) silane immobilized on metallic oxide-based nanoparticles for conjugation with cell targeting agents.* J Am Chem Soc, 2004. **126**(23): p. 7206-11.

37. Nitin, N., et al., *Functionalization and peptide-based delivery of magnetic nanoparticles as an intracellular MRI contrast agent.* J Biol Inorg Chem, 2004. **9**(6): p. 706-12.

38. Hermanson, G.T., *Bioconjugate Techniques*. 2008 (2nd ed.), San Diego: Academic Press. 1323.

39. Shen, T., et al., *Monocrystalline Iron-Oxide Nanocompounds (Mion) - Physicochemical Properties.* Magnetic Resonance in Medicine, 1993. **29**(5): p. 599-604.

40. Lee, H., et al., *Thermally cross-linked superparamagnetic iron oxide nanoparticles: synthesis and application as a dual imaging probe for cancer in vivo.* J Am Chem Soc, 2007. **129**(42): p. 12739-45.

41. Woo, K. and J.W. Hong, *Surface modification of hydrophobic iron oxide nanoparticles for clinical applications.* Ieee Transactions on Magnetics, 2005. **41**(10): p. 4137-4139.

42. Harris, T.J., et al., *Protease-triggered unveiling of bioactive nanoparticles.* Small, 2008. **4**(9): p. 1307-12.

43. Simberg, D., et al., *Differential proteomics analysis of the surface heterogeneity of dextran iron oxide nanoparticles and the implications for their in vivo clearance.* Biomaterials, 2009. **30**(23-24): p. 3926-33.

44. Barrera, C., A.P. Herrera, and C. Rinaldi, *Colloidal dispersions of monodisperse magnetite nanoparticles modified with poly(ethylene glycol).* J Colloid Interface Sci, 2009. **329**(1): p. 107-13.

45. Kingshott, P. and H.J. Griesser, *Surfaces that resist bioadhesion.* Current Opinion in Solid State & Materials Science, 1999. **4**(4): p. 403-412.

46. Woo, K., et al., *Easy synthesis and magnetic properties of iron oxide nanoparticles.* Chemistry of Materials, 2004. **16**(14): p. 2814-2818.

47. Kim, B.S., et al., *Magnetomicelles: composite nanostructures from magnetic nanoparticles and cross-linked amphiphilic block copolymers.* Nano Lett, 2005. **5**(10): p. 1987-91.

48. Ai, H., et al., *Magnetite-loaded polymeric micelles as ultrasensitive magnetic-resonance probes.* Advanced Materials, 2005. **17**(16): p. 1949-+.

49. Napoli, A., et al., *Lyotropic behavior in water of amphiphilic ABA triblock copolymers based on poly(propylene sulfide) and poly(ethylene glycol).* Langmuir, 2002. **18**(22): p. 8324-8329.

50. Rehor, A., J.A. Hubbell, and N. Tirelli, *Oxidation-sensitive polymeric nanoparticles.* Langmuir, 2005. **21**(1): p. 411-417.

51. Segura, T. and J.A. Hubbell, *Synthesis and in vitro characterization of an ABC triblock copolymer for siRNA delivery.* Bioconjug Chem, 2007. **18**(3): p. 736-45.

52. O'Neil, C.P., et al., *Extracellular matrix binding mixed micelles for drug delivery applications.* J Control Release, 2009. **137**(2): p. 146-51.

53. Christian, G.D., *Analytical chemistry*. 5th ed. 1994, New York: Wiley & Sons. xx, 812 p.

54. He, R., et al., *Core/shell fluorescent magnetic silica-coated composite nanoparticles for bioconjugation.* Nanotechnology, 2007. **18**(31): p. -.

55. Wang, D.S., et al., *Superparamagnetic Fe2O3 Beads-CdSe/ZnS quantum dots core-shell nanocomposite particles for cell separation.* Nano Letters, 2004. **4**(3): p. 409-413.

56. Salgueirino-Maceira, V., et al., *Composite silica spheres with magnetic and luminescent functionalities.* Advanced Functional Materials, 2006. **16**(4): p. 509-514.

57. Oh, H.T., et al., *Dynamic Stokes shift of dye molecules in glass-forming materials.* Journal of Luminescence, 1995. **66-7**(1-6): p. 310-314.

58. Perez, J.M., et al., *DNA-based magnetic nanoparticle assembly acts as a magnetic relaxation nanoswitch allowing screening of DNA-cleaving agents.* Journal of the American Chemical Society, 2002. **124**(12): p. 2856-2857.

59. LaConte, L.E.W., et al., *Coating thickness of magnetic iron oxide nanoparticles affects R-2 relaxivity.* Journal of Magnetic Resonance Imaging, 2007. **26**(6): p. 1634-1641.

60. Lee, J.H., et al., *Artificially engineered magnetic nanoparticles for ultra-sensitive molecular imaging.* Nat Med, 2007. **13**(1): p. 95-9.

61. Ahola, V., et al., *Model-based prediction of sequence alignment quality.* Bioinformatics, 2008. **24**(19): p. 2165-71.